Sixth International Symposium on Turbulence and Shear Flow Phenomena
Seoul, Korea, 22-24 June 2009

Rapid modification of the flow field about a free moving airfoil by controlled, trapped vorticity concentrations

Dan Brzozowski
Woodruff School of Mechanical Engineering
Georgia Institute of Technology
Atlanta, Georgia, USA
danb@gatech.edu

Ari Glezer
Woodruff School of Mechanical Engineering
Georgia Institute of Technology
Atlanta, Georgia, USA
ari.glezer@me.gatech.edu

ABSTRACT

The dynamic coupling between trailing edge flow control and the unsteady motion of a maneuvering airfoil is investigated in wind tunnel experiments. The airfoil is mounted on a 2-DOF traverse and the commanded maneuvers are effected without moving control surfaces. Bi-directional changes in the pitching moment over a range of angles of attack are effected by controllable, nominally-symmetric trapped vorticity concentrations on both the suction and pressure surfaces near the trailing edge. Manipulation and regulation of vorticity concentrations are effected by hybrid actuators comprised of a miniature [O(0.01c)] obstruction integrated with synthetic jet actuators.

INTRODUCTION

Closed-loop flow control strategies for maneuvering of small UAV platforms without moving control surfaces through a vorticity-centric approach to unsteady aerodynamics has been recently demonstrated in a series of wind tunnel (Kutay et al., 2007, Muse et al., 2008). The rapid maneuver and gust rejection capabilities mean that the maneuver time scales associated with vehicle dynamics are of the same order as the flow time scales. Control authority can be realized by fluidic modification of the "apparent" aerodynamic shape of the surface which exploits interactions between arrays of surface-mounted fluidic actuators and the local cross flow to form trapped vorticity concentrations that are regulated by the actuation. When these interaction domains are formed upstream of flow separation, the alteration of the local pressure gradients can result in complete or partial suppression of separation (Amitay et al. 1998, 2001, Amitay and Glezer 2002, and Glezer et al. 2005). Moreover, trapped vorticity flow control can also be effective when the baseline flow is fully attached. Chatlynne et al. (2001) and Amitay et al. (2001) showed that the formation of a stationary trapped vortex above an airfoil at low angles of attack leads to pressure drag reduction that is comparable to the magnitude of the pressure drag of the baseline configuration with minimal lift penalty. This approach was expanded by DeSalvo et al. (2002) and later by DeSalvo and Glezer (2004, 2005) to manipulate the Kutta condition of an airfoil by controlled concentrations of trapped vorticity near the trailing and leading edges using a miniature O(0.01c) hybrid actuator. The changes in the flow near the trailing edge result in a controllable increase in pitching moment. More recently, DeSalvo and Glezer (2007) reported bi-directional changes in pitching moment by nominally-symmetric trapped vorticity on both the suction and pressure surfaces.

Bi-directional control of the pitching moment using trapped vorticity near the trailing edge was recently exploited by Muse et al., (2008) and Brzozowski and Glezer (2008) to effect closed-loop, commanded 2-DOF maneuvers (pitch and plunge) of a free airfoil in a wind tunnel. The plunge motion of the trimmed model is controlled in force mode to maintain the static trim force on the model, and alter its effective mass while the model's dynamic characteristics are altered in pitch. Attitude stabilization and position control are achieved by closing a position loop using the flow control actuators.

The present paper focuses on the effect of actuator chord-wise position on the magnitude of trapped vorticity concentration and the resulting induced aerodynamic forces and moments. The effects of the dynamic response of the model to trailing edge trapped vorticity actuation for a desired maneuver under closed loop control is compared to the dynamics associated with externally-applied pure torque actuation that yields the same model trajectory.

EXPERIMENTAL SETUP

The experiments are conducted in an open-return low-speed wind tunnel having a square test section measuring 1 m on the side using a modular 2-D airfoil model based on a NACA 4415 configuration (c = 457 mm, t/c = 0.15, S = 728 mm). The model includes a circumferential array of 70 static pressure ports at mid-span, and several high-frequency integrated pressure sensors. Bi-directional pitching moments induced by trapped vorticity flow-control is effected by individually-controlled, hybrid surface actuators (characteristic height of 0.017c above the airfoil) integrated with rectangular (orifice width 0.4 mm) high aspect ratio synthetic jets (DeSalvo and Glezer 2004) that are mounted on the pressure and suction surfaces (*PS* and *SS*, respectively) near the trailing edge (Figure 1). The jets are driven by piezoelectric membranes operated off resonance at f_{act} = 2050 Hz. The bulk of the present experiments are conducted at a free stream speed of U_∞ = 30 m/s, with $Re_c = 8.55 \cdot 10^5$, $St_{act} = f_{act}c/U_\infty = 34$, and $C_\mu = 1 \cdot 10^{-3}$.

The wind tunnel model executes commanded flight maneuvers in two degrees of freedom (pitch and plunge) that are exclusively effected by flow control actuation (Muse et al., 2008). The model is mounted on a programmable, 3-DOF (pitch, plunge, and roll) traverse driven electromechanically by a dedicated feedback controller that removes the effect of parasitic mass and

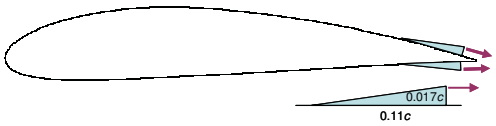

Figure 1. Schematic of the NACA 4415 airfoil with hybrid actuators on each surface near the trailing edge.

rotational inertia of the dynamic support system using integrated force sensor and accelerometers. Pitch commands are executed by an AC servo motor that is attached to one of the vertical stages. Vertical forces are regulated by two independently-controlled vertical linear slides.

RESULTS AND DISCUSSION

Variations of Trapped Vorticity

As noted above, maneuvering in pitch and plunge is accomplished through bi-directional, dynamic modification of the aerodynamic pitching moment by exploiting controllable, trapped CW and CCW vorticity concentrations on the suction and pressure surfaces near the trailing edge. The changes in the vorticity field are accompanied by substantial changes in the pressure distributions near the trailing edge and consequently in both C_L and C_M which can be adjusted over a broad range of angles of attack by varying the actuation jet momentum coefficient C_μ. In particular, the operation of hybrid actuators on the pressure (*PS*) or suction (*SS*) sides of the airfoil leads to nose-up or nose-down pitching moments, respectively relative to the unactuated configuration and is limited by the generated changes in C_M. The earlier work of DeSalvo and Glezer (2007) indicated that the control authority over C_M is sensitive to the location of the actuators relative to the trailing edge. Starting from a configuration in which both the pressure and suction side actuators are mounted at the same distance from the trailing edge, ($x_{SS} = x_{PS} = 0.98c$), the control authority of the actuators over a range of angles of attack is measured by the trim vertical force and torque increments using the inner loop controller when the actuators are fully activated relative to the corresponding aerodynamic force and moment in the absence of actuation.

Figure 2a shows the variation of the induced moment increment ΔC_M (relative to the baseline in the absence of actuation) with angle of attack ($-2^o < \alpha < 10^o$). The *SS* and *PS* actuators are mounted at $x_{SS} = x_{PS} = 0.98$ and operated separately (at full actuation level $C_\mu \approx 2 \cdot 10^{-3}$). These data show that the favorable pressure gradient on the pressure surface leads to a thinner boundary layer and therefore enhanced effectiveness of the actuation there and, as a result, the (positive, nose-up) pitching moment increases with α. Because of the thickening of the boundary layer on the suction surface owing to the adverse pressure gradient, the (negative, nose-down) pitching moment induced by *SS* actuation decreases with α. As a result of the difference between the (almost linear) variation of $\Delta C_{M,SS}$ $\Delta C_{M,PS}$ with α, the moment increment between the *SS* and *PS* actuators increases linearly with α by about 20% over the present range.

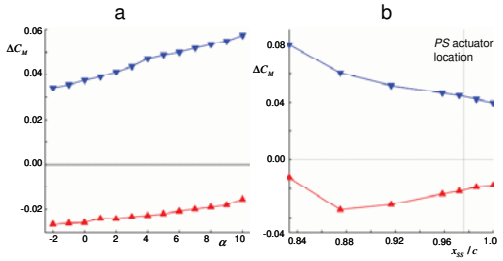

Figure 2. a) Variation of pitching moment increment (about the axis of rotation) at full actuator power with angle of attack (actuators at $x_{PS} = x_{SS} = 0.98c$). b) Variation of pitching moment at full actuator power with *PS* actuator position: ▼ *PS* and ▲ *SS* actuation.

The sensitivity of the induced pitching moment to actuator position is investigated over a range of streamwise positions x_{SS} and x_{PS}. Figure 2b show the variation of ΔC_M for $\alpha = 3^o$ $x_{PS} = 0.98c$, and $0.83 < x_{SS}/c < 1$. As the *SS* actuator is moved upstream from the trailing edge, the magnitude of ΔC_M increases and reaches a local maximum at $x_{SS} = 0.875c$ where $\Delta C_M = -0.035$ which is about 52% higher than the corresponding ΔC_M at $x_{SS} = 0.98c$. It appears that although the *SS* boundary layer does not change significantly, the larger distance from the trailing edge allows for the trapping of a higher concentration of CW vorticity. This is also evident from the corresponding increment in the lift coefficient ΔC_L which increases from 0.07 (for $x_{SS} = 0.98c$) to 0.13 (for $x_{SS} = 0.875c$). This effect diminishes when the distance from the trailing edge increases to $x_{SS} = 0.83c$. It is remarkable, that while the magnitude of ΔC_M increases with the decrease in x_{SS}, the magnitude of the pitching moment that is induced by the *PS* actuator also increases monotonically even though $x_{PS} = 0.98c$ remains invariant. In fact, for $x_{SS} = 0.83c$ ΔC_M that is induced by the *PS* actuator nearly doubles from 0.040 to 0.080. At the same time, the magnitude of the decrement in lift (that is normally associated with trapping of CCW vorticity by the *PS* actuator) also increases (by about 50%) indicating an increased ability to trap vorticity by the PS actuator. Given the present results and a similar investigation of the sensitivity to x_{PS}, it was decided to place the actuators at $x_{SS} = 0.875c$ and $x_{PS} = 0.972c$.

The variation of the pitching moment about the axis of rotation, $C_{M,a}$, with the normalized actuation input level u_f was measured over a range of angles of attack $-2^o < \alpha < 10^o$ (Figure 3, where *SS* actuation is marked by upside triangles). It is noteworthy that while ΔC_M increases almost monotonically with u_f for the *PS* actuators, the *SS* actuation exhibits some latency for $u_f < 0.2$ indicating a threshold in effectiveness that is probably associated with the thicker boundary layer on the suction surface as discussed above. In fact, at low α, the *SS* actuators generate a slight nose-up pitching moment. As expected, the effectiveness of the actuation on the suction side decreases with increasing α and the magnitude of the maximum moment increment ($\Delta C_{M,a} = -0.03$, nose-down) is about 60% of the corresponding moment on the pressure side (0.05, nose-up). These trends hold over nearly the entire attached flow regime. It should be noted that the nonlinearities of the moment increments with u_f can be compensated for in the implementation of the system controller.

The effect of the actuation on the time-averaged flow in the wake is assessed from time-averaged PIV measurements in the domain $0.85 < x/c < 1.15$ and $-0.15 < y/c < 0.15$ for $\alpha = 3^o$ [where $(x/c, y/c) = (1,0)$ corresponds to the location of the trailing edge at this angle]. The filed of view includes the exit plane of the *SS* actuation jet while the *PS* actuator is masked by the shadow of the laser sheet. Figure 4a-e shows raster plots of distributions of the normalized spanwise vorticity distributions $\omega/(c/U_0)$ and velocity vectors for the baseline flow (i.e., in the absence of actuation, Figure 4c) and for *SS* actuation ($u_f = 1$, and 0.5, Figures 4a-b,

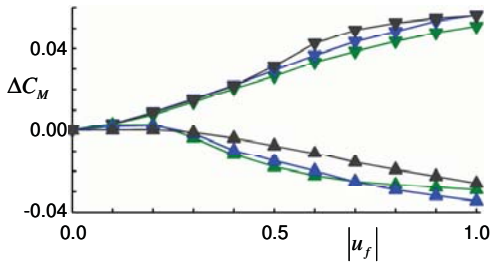

Figure 3. Variation in pitching moment increment with (normalized) actuation level: ▼ *PS* and ▲ *SS* actuation at α = -2°, 3°, and 10°.

respectively) and *PS* actuation (u_f = -0.5, and -1, Figures 4d-e, respectively).

As described in §2, the each actuator comprises a spanwise ramp-like obstruction (having a characteristic height of 0.02*c*) that is integrated with a spanwise array of synthetic jet actuators whose orifice is placed along the downstream end of the ramp blowing tangential to the freestream over a rounded Coanda-like surface (cf., DeSalvo and Glezer, 2007). In the absence of actuation (Figure 4c) the baseline flow separates locally over the downstream edge of each of the *SS* and *PS* actuator ramps and forms closed recirculation domains between each actuator and the trailing edge. This recirculation domain has vorticity of the same sense as in the approaching boundary layer (namely, CW and CCW for *SS* and *PS*, respectively). Although the flow near the surface of the airfoil upstream of the trailing edge is not fully resolved, it is possible to discern a CCW vorticity layer near the surface that is associated with the presence of the reversed flow. By regulating the size and strength of these recirculation zones, it is possible to alter the global aerodynamic forces and moments on the airfoil. In the absence of actuation, the near wake downstream of the trailing edge is formed by the merging of the vorticity layers from both sides of the airfoil.

Activation of the *SS* actuators (Figures 4a-b) causes the flow downstream of the actuator to tilt towards the surface reducing the thickness of the vorticity layer and minimizing or eliminating the recirculating flow. While the strength of the vorticity immediately downstream of the exit plane of the actuator remains almost unchanged compared to the unforced flow (Figure 4c), there is a profound reduction in the strength and thickness of the vorticity concentrations downstream of the actuator and in the near wake that are proportional to the strength of the actuation. Furthermore, the collapse of the separated domain is accompanied by downward vectoring of the local flow and a significant reduction in the cross stream width of the wake (about 80% compared to the unforced flow). This downwash is consistent with the increase in circulation and lift as discussed above and the increase in nose-down pitching moment (as discussed in connection with Figure 7 below, see also Muse et al., 2008). Although the flow domain immediately downstream of the *PS* actuators is obscured by the shadow of the airfoil, the vorticity maps in Figures 4d-e it is clear that the effects of the *PS* and *SS* actuations are similar. The operation of the *PS* actuators causes the CCW vorticity layer on the pressure side become somewhat thinner and leads to an upwash of the near wake that is associated with the reduction in the lift and a decrease in the nose-down pitching moment. Unlike the SS actuation, PS actuation does not lead to a significant change in the cross-stream width of the near wake and also results in local thickening of the CW vorticity layer upstream of the trailing edge.

Since the regulation of the vorticity concentrations and trapping is crucial to the present control approach, we now turn attention to the effects of the actuation on the vorticity flux in the wake. The time-averaged vorticity flux, $\bar{f} = \bar{u}\,\bar{\omega} + \overline{u'w'}$ is computed from the measured velocity field in the *x*-*y* plane (neglecting the turbulent convection term) and is extracted within the near wake at the streamwise station x/c = 1.06. Cross stream distributions of the vorticity flux are plotted over a range of actuation levels of the *SS* and *PS* actuators (Figure 5). Note that in the absence of a change in the lift, the integral of the vorticity flux across the wake must vanish. The distributions of the vorticity flux in the presence of actuation exhibit two distinct features. First, the presence of actuation results in significant broadening of the flux component from the forced side of the airfoil although the broadening that is associated with the *SS* actuation is considerably stronger. Second, during the transition from *SS* to *PS* actuation the flux peaks within the near wake migrate about 0.039*c* upward on the suction side and about 0.024*c* on the pressure side which are indicative of the reduction in lift. However, it is noteworthy that the change in the elevation of the center of the wake as measured by the zero crossing of the vorticity flux (Figure 6) is almost symmetric with excursions of 0.015 and -0.018. As noted in connection with Figure 5, the response of the flow to *SS* and *PS* actuation is asymmetric. The distortion of the flux distribution caused by the two actuators shows how the actuators couple to the flow downstream of the trailing edge. The *SS* actuators which lead to a lower increment in pitching moment (but not in C_L) cause a larger reduction in the magnitude of vorticity flux through the wake compared to the *PS* actuators.

The corresponding lift and pitching moment increments ΔC_L and $\Delta C_{M,\,c/4}$ (relative to *c*/4) are plotted in Figure 7 for all the available data (about 3,000 points) within the range -2° < α < 10°, normalized actuation amplitude -1 < u_f < 1, and actuator positions x_{PS} and x_{SS}. It is remarkable that the entire data set collapses on a single linear distribution with a slope of $\partial\Delta C_L/\partial\Delta C_{M,c/4}$ = -3.2 (for a thin airfoil

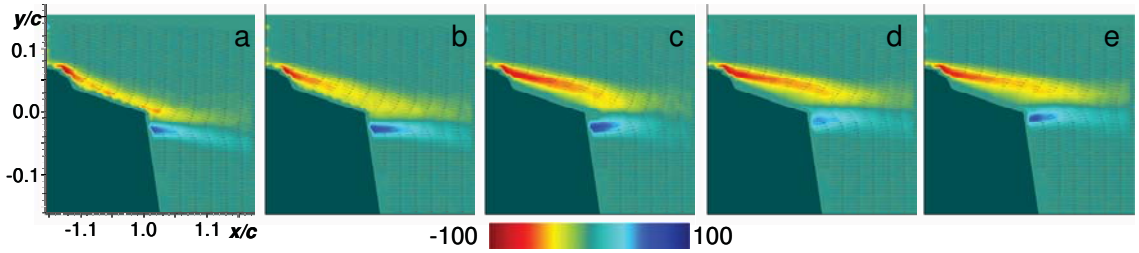

Figure 4. Time-averaged vorticity field in the near wake with overlaid velocity vectors at α = 3° for *SS* actuation: u_f = 1 (a), and u_f = 0.5 (b), no actuation (u_f = 0, c), and *PS* actuation: u_f = -0.5 (d), and u_f = -1 (e).

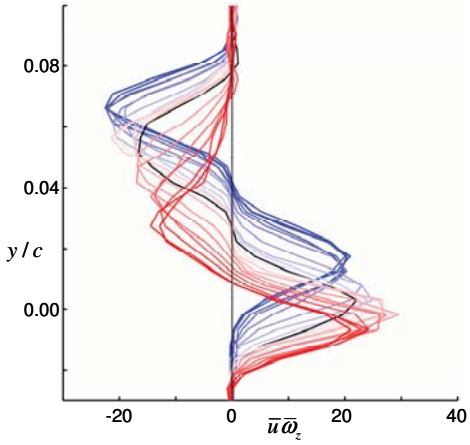

Figure 5. Streamwise flux of spanwise vorticity though the wake at $x/c = 1.06$ for a range of actuation levels $-1 < u_f < 1$ (*SS*, *PS*, baseline) color intensity increases with actuation level.

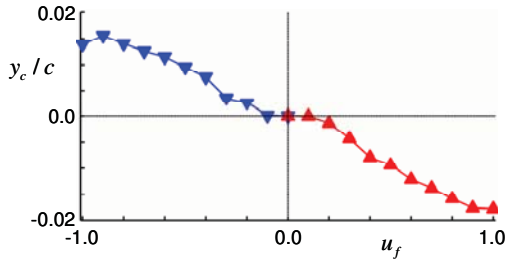

Figure 6. Variation of center wake (defined by $\omega_z = 0$) deflection with *PS* (▼) and *SS* (▲) actuation.

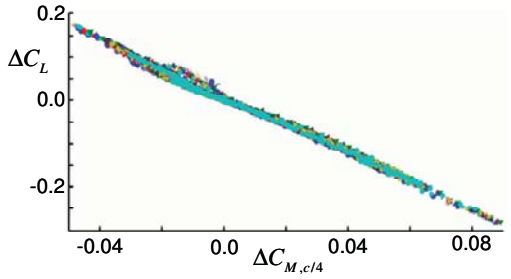

Figure 7. Variation of actuation-induced increments in lift and pitching moment (about the $c/4$) for a 3000-point data set over a range of u_f, α, and (x_{PS} and x_{SS}).

$\partial C_L/\partial C_{M,c/4} = -4$). That different actuation effects, as manifested by changes in actuation position and actuation strengths at all angles of attack, collapse on a single curve, indicates that the increments in the lift and pitching moment are primarily affected by the strength of the trapped vorticity.

Unsteady dynamic interactions

The dynamic interaction of trapped vorticity actuation with the unsteady flow about a maneuvering airfoil is investigated during feedback control. The airfoil is commanded to track a sinusoidal trajectory given by $\alpha = \alpha_o + \alpha_1 \sin(2\pi ft)$, where $\alpha_o = 3^o$, $\alpha_1 = 0.5^o$, and $f = 6.25$ Hz. During the maneuver, the angular attitude, angular acceleration, the torque applied by the servo motor, vertical position and acceleration of each side of the model, vertical force on each side of the model are monitored and recorded in phase with the pitch trajectory command. To elucidate the unsteady aerodynamic effects that are associated with the motion of the airfoil under flow control, an identical commanded trajectory is also executed using "external torque" that is applied by the servo motor. To this end, it is desired to compare four different actuation programs namely, maneuvers with the flow control actuators and with "external torque", and corresponding static control (i.e., the model is held motionless) over a range of angles of attack with the two types of actuation. It is noted in passing that torque control has been traditionally used for effecting unsteady maneuvers in pitch in wind tunnel experiments usually for investigations of dynamic stall (e.g., Gerontakos and Lee, 2004).

To begin with, PIV measurements in the near wake (similar to Figure 4) are taken phase locked to the airfoil's trajectory for each of the two dynamic actuation modes, and for the corresponding static cases over the same range of angle of attack that is attained by the moving model. Figures 8a-d are phase-averaged (a-b) or time-averaged (c-d) vorticity maps at $\alpha_{nominal} = 2.84^o$ ($\phi = 325^o$, pitch -up) when the model is controlled by the fluidic actuators (a), external torque (b) static-actuators (c) and static-torque (d). Perhaps the most striking feature of these images is that while there are significant differences between the dynamic and static vorticity maps under flow control (Figures 8a&c, respectively), there is almost no difference between the static and dynamic maps when the model is under torque control (Figures 8b&d). The vorticity maps in Figures 8a&c indicate that although the actuation level of the *SS* actuators (as this phase) is the same ($u_f = 0.41$) the CW vorticity layer on the static model is closer to the surface (indicating a smaller recirculation domain) and the streamwise diminution of the vorticity towards the trailing edge is stronger. Furthermore, in concert with the nose-up motion of the airfoil, the CCW vorticity layer is tilted upward and the wake is wider compared to the stationary airfoil. It is also interesting to note that there are differences in vorticity concentrations within the wake between Figures 8a&c and b&d. Even though the *PS* and *SS* actuators are inactive under torque control, the vorticity concentrations for $x/c > 1.1$ are considerably more diffused compared to the actuated cases.

The dynamics effects of the two actuation modes on the velocity field in the near wake are assessed from the relative (or "residual") velocity fields between the dynamic and the corresponding static distributions $\bar{\mathbf{u}}_{res} = \bar{\mathbf{u}}_{dynamic} - \bar{\mathbf{u}}_{static}$ for flow and torque control (Figures 8e&f, respectively). While there are no evident dynamic effects when the airfoil is controlled with external torque, under flow control the wake is shifted upward and there is a reduction in the velocity over the *SS* upstream of the trailing edge. Given that the *SS* actuators are active during this part of the maneuver (which results in downward vectoring of the near wake for the static airfoil), the upward tilting indicates a change in the structure of the trapped vorticity near the trailing edge and of the Kutta condition that is associated with the evolution of the unsteady aerodynamic forces (including a phase change between the actuator command and the resulting forces as discussed in connection with Figure 10). The differences in the evolution of the unsteady forces between the dynamic and static cases is further evident in the corresponding vorticity fluxes (Figure 9, $x/c = 1.06$) which demonstrates that the flux of the CW vorticity is significantly stronger in the dynamic case suggesting an

increase in the circulation and therefore in the unsteady lift. Figure 9 also shows that the differences in vorticity flux between the static and dynamic modes of the torque control are negligible.

Figure 10 is a comparison between the time-dependent aerodynamic response of the airfoil to actuation with flow control (a-f) and with external torque (f-j) during three cycles of the commanded attitude $\alpha(t)$ (realized attitude if show in in Figures 10a&f). The command signals to the actuators and torque motor are shown in Figures 10b&g. Note that as part of this maneuver, the model's effective moment of inertia is reduced using feedback of the (measured) angular acceleration while flow controlled attitude is effected exclusively by the flow control actuators. As shown in Figure 10b, the actuation reaches the maximum level that is available from the present actuators when the model is moving between zero crossings and the peaks of α. Comparison with the static airfoil (for the two actuation modes) utilizes a look-up table of static $C_M(\alpha, u_f)$, $C_L(\alpha, u_f)$ that correspond to instantaneous $\alpha(t)$ and $u_f(t)$ of the dynamic models (shown using dashed lines in Figures 10c-e).

The instantaneous lift is estimated from the measured reaction forces and linear accelerometers, $F_L = m\ddot{y} - F_R$, where m is the mass of the suspended model and appendages. The lift is shown in Figure 10c along with the corresponding "static" lift obtained from the lookup table. The most remarkable feature of the lift traces is the magnitude of the dynamic excursions that about twice the magnitude of the

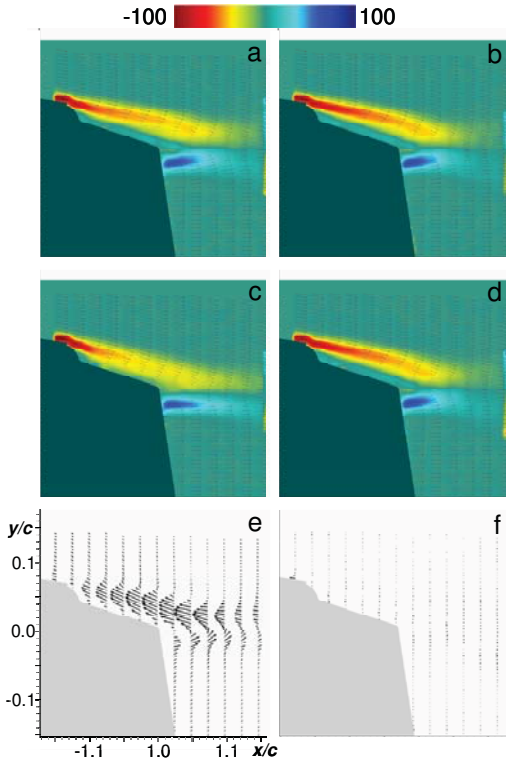

Figure 8. Phase-averaged vorticity maps when the model is driven in pitch by flow control (a), external torque (b), and the corresponding maps for static model (c and d, respectively). Maps of the relative velocity vectors between the dynamic and static model are shown in (e) and (f), respectively.

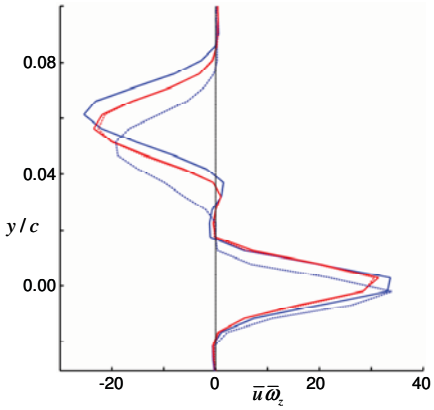

Figure 9. Streamwise flux of spanwise vorticity though the wake at $x/c = 1.06$ for corresponding to Figure 8(a-d). Traces for the moving model and corresponding static model are shown in solid lines) (dashed lines) under flow control (blue) and external toruqe (red).

static values, owing to the unsteady effects associated with the model time-dependent attitude. It is also noteworthy that the corresponding time traces of the lift for the torque controlled model (Figure 10h) are nearly constant (which is consistent with negligible change in static lift over this small change in α).

The instantaneous aerodynamic pitching moment is estimated from time histories of the servo torque and angular acceleration: $T_{aero} = I_z\ddot{\alpha} - T_{servo}$, where I_z is the moment of inertia about the pitch axis. Note that the "plateaus" in the computed "static" values (e.g., $60 < t < 103$ ms and $146 < t < 186$ ms in Figure 10c) correspond to the saturation of the control signal. The dynamic pitching moment lags the static value by 18 ms which corresponds to 1.2 convective time scales, and is indicative of the characteristic time scale that is needed for the flow to adjust to the changes in attitude. The corresponding traces for the torque-controlled model clearly show that the negligible differences between the dynamic and static flow fields (Figures 8f&9) translate to vanishingly small dynamic pitching moment under torque control.

Finally, the phase-averaged net vorticity flux through the wake ($x/c = 1.06$) is estimated from the PIV measurements over the commanded time-harmonic attitude period (the cycle is repeated three times in each of Figures 10e&j along with flux measurements from corresponding static cases at same α and u_f). The net flux for the static airfoil should vanish and so the time variations in the traces of the static airfoil indicate that the cross stream extent of the measurements probably does not capture the full flux. While there is little variation between the fluxes of the torque controlled traces, there is a strong negative peak immediately following the transition from *SS* to *PS* actuation, which is consistent with a shedding of CW (negative) vorticity into the wake as the *SS* actuators are disengaged and the trapped vorticity is shed away. These peaks also correspond to the momentary strong reduction unsteady lift that are evident in Figure 10c.

CONCLUSIONS

The dynamic coupling between trailing edge flow control and the unsteady motion of a maneuvering airfoil is investigated in wind tunnel experiments. Bi-directional changes in the pitching moment over a range of angles of

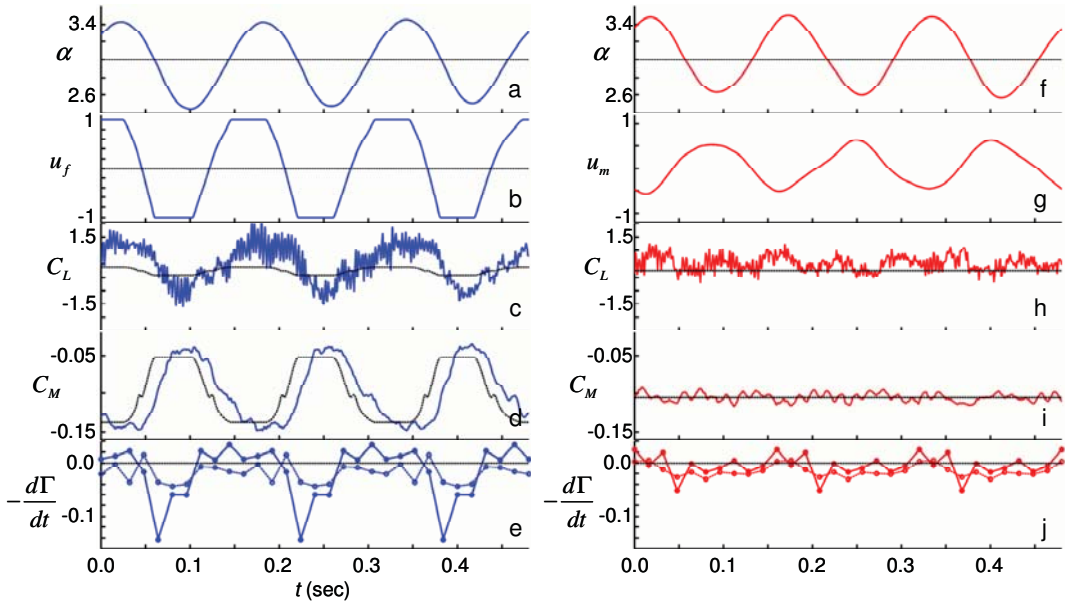

Figure 10. Comparison of the time-dependent aerodynamic response of the airfoil to actuation with flow control (left column, a-f) and with external torque (right column, f-j). Time histories of: attitude trajectory α(t) (a, f), actuator command (a, g), C_L(t) (c, h), pitching moment (d, i), and vorticity flux (e, j). Corresponding aerodynamic responses for the static airfoil are plotted in (c, d, h, i). .

attack are effected by trapped vorticity concentrations that are induced by hybrid actuators on the suction and pressure surfaces near the trailing edge. It is shown that the resulting aerodynamic moment is sensitive to the actuators' streamwise position and that the magnitude of the pitching moment increment effected by the *PS* and *SS* actuation increases by nearly 50% and 80%, respectively. Moreover, the lift and pitching moment increments ΔC_L and $\Delta C_{M,\,c/4}$ (relative to *c*/4) for a broad range of data (angle of attack, actuation level and position) collapses on a single linear distribution with a slope of $\partial\Delta C_L/\partial\Delta C_{M,c/4} = -3.2$. This collapse indicates that the lift and pitching moment increments are primarily affected by the strength of the trapped vorticity.

The dynamic interaction of trapped vorticity actuation with the unsteady flow about a maneuvering airfoil is investigated during feedback control. To elucidate the unsteady aerodynamic effects that are associated with the motion of the airfoil under flow control, two different actuation programs with flow control actuators and with "external torque" and their corresponding static control (when the model is held motionless) are compared during a prescribed maneuver. It is found that while the effects of external torque on the dynamic and static model are almost identical, flow control actuation leads to significant differences in the instantaneous pitching moment, lift, and vorticity flux between the dynamic and static flow fields. These differences between the torque and flow control substantiate the strong coupling between the actuation, changes in the flow field about the airfoil and the motion of the model.

REFERENCES

Amitay, M. and Glezer, A., 2002, "Controlled Transients of Flow Reattachment over Stalled Airfoils," *Int. J. Heat Trans. Fluid Flow*, **23**.

Amitay, M., Horvath, M., Michaux, M., and Glezer, A., 2001, "Virtual Aerodynamic Shape Modification at Low Angles of Attack using Synthetic Jet Actuators," AIAA-2001-2975.

Amitay, M., Smith, B. L., and Glezer, A., 1998, "Aerodynamic flow control using synthetic jet technology," AIAA-98-0208.

Chatlynne, E., Rumigny, N., Amitay, M., and Glezer, A., 2001, "Virtual Aero-Shaping of a Clark-Y Airfoil using Synthetic Jet Actuators," AIAA-2001-0732.

DeSalvo, M., Amitay, M., and Glezer, A., 2002, "Modification of the Aerodynamic Performance of Airfoils at Low Angles of Attack: Trailing Edge Trapped Vortices," AIAA-2002-3165.

DeSalvo, M. and Glezer, A., 2004, "Aerodynamic Performance Modification at Low Angles of Attack by Trailing Edge Vortices," AIAA-2004-2118.

DeSalvo, M. and Glezer, A., 2005, "Airfoil Aerodynamic Performance Modification using Hybrid Surface Actuators," AIAA-2005-0872.

DeSalvo, M. and Glezer, A., 2007, "Control of Airfoil Aerodynamic Performance Using Distributed Trapped Vorticity," AIAA-2007-0708.

Glezer, A. and Amitay, M., 2002, "Synthetic Jets," *Ann. Rev. Fluid Mech.*, **24**.

Gerontakos, P. and Lee, T., 2004, "Investigation of Flow Over an Oscillating Airfoil," *J. Fluid Mech.*, **512**.

Kutay, A. T., Culp, J. R., Muse, J. A., Brzozowski, D. P., Calise, A. J., and Glezer, A., 2007, "A Closed-Loop Flight Control Experiment Using Active Flow Control Actuators," AIAA Paper 2007-114.

Muse, J. A., Kutay, A. T., Brzozowski, D. P., Calise, A. J., and Glezer, A., 2008, "Dynamic Flight Maneuvering Using Trapped Vorticity Flow Control," AIAA Paper 2008-0522.

Smith, B. L. and Glezer, A., "The Formation and Evolution of Synthetic Jets," *Phys Fluids*, **10**, 1998.